Carbon 108 (2016) 291–302

Contents lists available at ScienceDirect

Carbon

journal homepage: www.elsevier.com/locate/carbon

Mechanical energy dissipation modeling of exfoliated graphite based on interfacial friction theory

Lifeng Xiao [1], D.D.L. Chung*

Composite Materials Research Laboratory, University at Buffalo, State University of New York, Buffalo, NY, 14260-4400, USA

ARTICLE INFO

Article history:
Received 18 April 2016
Received in revised form
20 June 2016
Accepted 24 June 2016
Available online 27 June 2016

ABSTRACT

Mechanical energy dissipation is important for vibration damping and sound absorption. This paper provides an analytical model for the interfacial-friction-based viscous behavior of exfoliated graphite, thereby establishing a methodology that may be applied to such behavior of materials in general. This model is in contrast to the conventional bulk viscous deformation model. It can be used to predict the viscous behavior (e.g., loss modulus) from the material properties. A dimensionless deformation factor is introduced to describe the off-axis dimensional change upon viscous deformation. The interfacial-friction-based energy loss is calculated from the equivalent friction force and equivalent sliding displacement, which are in phase during dynamic sinusoidal flexural loading. Each cell in exfoliated graphite is modeled as a pore bounded by Voigt-element-based cell walls, which have merged in order to form the cellular structure. The viscous behavior stems primarily from the sliding between the merged cell walls. The contribution of sliding between graphite layers within a cell wall is negligible. The greater is the solid content, the smaller is the displacement, the higher is the friction force, the less is the energy loss and the lower is the degree of viscous character. Excellent agreement is obtained between the modeling and experimental results.

1. Introduction

The viscous and mechanical-energy-dissipating behavior of materials is needed for vibration damping [1], mechanical energy dissipation (energy loss), mechanical isolation, sound absorption, gasketing and sealing, which are important for the durability, safety, operation and performance of structures and systems. Moreover, vibration reduction and sound absorption are valuable for improving the quality of life of people. This paper does not address sound absorption, gasketing or sealing explicitly, but the theory developed may be useful for sound absorption, gasketing and sealing as well, in spite of the difference in frequency between sound and vibration waves.

The viscous behavior of viscoelastic materials such as rubber and other polymers is well-known and is due to the bulk viscous deformation that is enabled by the molecular structure of these materials [2]. However, these materials suffer from their low stiffness (elastic modulus), which results in their ineffectiveness for vibration damping (i.e., mechanical energy dissipation), though they are effective for mechanical isolation by serving as a cushion. Moreover, the viscous character of polymers is strongly dependent on the temperature, with the viscous character being strong only over a narrow temperature range, such as temperatures around the glass transition temperature. In contrast, carbons have much weaker temperature dependence of their viscous behavior. This weak temperature dependence means that the viscous character can be appreciable over a wide range of temperatures, including room temperature, which is particularly important for structural applications such as airframe, automobile, wind turbines, helmets, etc.

The interfacial-friction-based viscous mechanism involves friction-related slippage at interfaces. It is different from the bulk viscous deformation mechanism. It requires a large interface area, such that the interfaces are loose enough to allow easy sliding. The large-area interfaces can be provided by the interfaces in a nanostructure. Prior work on this subject has addressed carbon nanotube polymer-matrix composites, with the interfaces being the nanotube-polymer interface and the nanotube-nanotube interface [3,4]. It has also addressed porous ceramic coatings [5] and steel

* Corresponding author.
E-mail addresses: xiaolifeng@buaa.edu.cn (Lifeng Xiao), ddlchung@buffalo.edu (D.D.L. Chung).
URL: http://alum.mit.edu/www/ddlchung
[1] Additional affiliation and permanent address: School of Mechanical Engineering and Automation, Beihang University, No. 37, Xueyuan Road, Haidian District, Beijing, PR China, 100191.

http://dx.doi.org/10.1016/j.carbon.2016.06.098
0008-6223/

reinforced concrete [6]. In contrast, this paper addresses exfoliated graphite (EG) [7,8], which has a cellular structure and is very different in structure from the materials of the abovementioned prior work. That EG exhibits exceptionally strong interfacial-friction-based viscous behavior has been recently reported [9,10], but no mathematical support has been provided for this mechanism in EG. Furthermore, exfoliated graphite exhibits elastomeric behavior, as shown by instrumented indentation testing [11].

Chen and Chung [9] reported strong viscous behavior (exceeding that of rubber) in the cell wall of the cellular structure of EG (compacted without a binder), with the viscous behavior believed to stem from the large area of the interfaces between the graphite layers in a 60-layer 20-nm cell wall. However, the details of the interfacial mechanism have not been addressed. The process of exfoliation has loosened the interfaces, thereby facilitating interfacial sliding [10].

"Flexible graphite" is EG that has been severely compacted uniaxially in the absence of a binder to form a sheet [7]. The sheet formation is enabled by the mechanical interlocking of the EG. The interlocking is made possible by the cellular structure of EG. The greater is the degree of mechanical interlocking, the smoother is the surface of the flexible graphite sheet [12]. This material is resilient in the direction perpendicular to the plane of the sheet [9,13], due to the preferred orientation of the graphite layers in the plane of the sheet (a consequence of the tremendous consolidation during the compaction) and the cellular structure that remains after the compaction. The resiliency of flexible graphite has been shown by the reversible change in the electrical resistivity in the through-thickness direction up to a compressive strain amplitude of 25% [13]. Due to this resiliency, flexible graphite is commercially used as a gasket material, particularly for chemically and thermally harsh environments. The effectiveness of flexible graphite as a gasket material indicates that suitably nanostructured carbons can be rendered to be appreciable in the viscous character. Although flexible graphite (resilient) has been in the market for decades as a gasket material, the science behind its resiliency has received little attention.

Each unit of EG, as obtained from a single intercalated graphite flake, is known as a worm. Due to their cellular structure, the worms interlock mechanically and form a monolithic solid. The sheet (flexible graphite) is commercially made by the severe compaction of worms in the absence of a binder. However, the compacted EG reported by Chen and Chung [9,11] is not as severely compacted as the flexible graphite, so that the interfacial sliding is easier and the viscous character is stronger. The viscous character of compacted EG decreases with increasing degree of compaction (i.e., increasing solid content) [9].

The viscous character of flexible graphite is not strong [14]. The character is much stronger in compacted EG fabricated by compaction at pressures that are much below those used in fabricating flexible graphite [9].

This paper is aimed at providing a mathematical model for elucidating the viscous behavior of exfoliated graphite. The model provides a methodology that may be applicable to other cellular materials as well.

2. Exfoliated graphite

Exfoliated graphite (EG) refers to graphite that has a degree of separation of a substantial portion of the carbon layers in the graphite. The EG exhibits clinginess, due to its cellular structure (Fig. 1(a) and (b)). The clinginess allows the formation of EG compacts and flexible graphite sheet without a binder. The exfoliation typically involves intercalation [15,16], followed by heating. Upon heating, the intercalate vaporizes and/or decomposes into smaller molecules, thus causing expansion and cell formation [17–19]. The sliding of the carbon layers relative to one another enables the cell wall to stretch (Fig. 1(b) and (c)). The exfoliation process is accompanied by intercalate desorption, so that only a small portion of the intercalate remains after exfoliation. The most widely used intercalate is sulfuric acid [20].

The intercalate is typically present in the form of islands, in accordance with the Daumas-Herold model [21], in which the graphite layers bend, thereby resulting in domains, each of which is an intercalate island (Fig. 1(d)). This model has been confirmed by electron microscopy [22,23]. It means that, for stages greater than 1, the intercalate layer does not necessarily extend all the way from one end of the graphite crystal to the other.

During the heating of intercalated graphite, each intercalate island expands tremendously along the c-axis of the graphite. The larger are the intercalate islands, the greater is the degree of expansion [17]. The expansion can be up to a few hundred times, [17,20,24,25]. The driving force of the expansion is the vaporization or decomposition of the intercalate upon heating [17,20].

In order for the large expansion to be able to occur during exfoliation, the graphite layers that make up the wall of an intercalate island must be able to stretch greatly (Fig. 1(d)). The stretching of the wall enables an intercalate island to expand like a balloon.

The degree of viscous behavior of the cell wall of exfoliated graphite has been measured to be extraordinarily high among solid materials, including bulk rubber [9]. The degree of viscous character is described by the loss tangent (i.e., $\tan\delta$, where δ is the phase angle (phase lag) between the stress wave and the strain wave during dynamic loading), which is equal to the ratio of the loss modulus to the storage modulus. During dynamic flexure (Fig. 2(a) and (b)) of an exfoliated graphite compact (formed by compressing pieces of exfoliated graphite, or worms, in the absence of a binder, with the worms connected during the compression through mechanical interlocking that is enabled by the cellular structure on the surface as well the interior of each worm), the loss tangent of the cell wall (as given approximately by the loss tangent of the compact divided by the solid volume fraction) has been determined experimentally to be up to 35 (Fig. 2(c), (d) and (e)) [9], compared to a value of 0.7 for bulk rubber [2]. The value of 35 is unprecedentedly high values among solid materials. The values decrease with increasing degree of compaction of the exfoliated graphite (i.e., with decreasing solid content in the compact) (Fig. 2(c), (d) and (e)), due to the associated decreasing ease of sliding between the layers as the compact becomes more tightly packed. This means that an adequate degree of looseness of the binding between the layers is required for the viscous behavior to be substantial. The extraordinarily high degree of viscous character is made possible by the interface-derived viscous mechanism under the condition that the layers are sufficiently loosely bound. This interfacial mechanism results in energy loss due to the friction between the layers as sliding occurs.

In contrast to the viscous character, the elastic character of the cell wall is essentially independent of the degree of compaction, weakening slightly with increasing degree of compaction (Fig. 2(b)) [9]. This means that the stiffness of the cell wall tends to decrease slightly with increasing solid content, presumably due to the defects generated in the graphite layers during compaction and the increase in the amount of defects as the compaction pressure increases. The loss modulus of the compact increases with increasing solid content; this trend correlates with the increase of the storage modulus of the compact with increasing solid content. However, the loss-modulus/solid-content decreases with increasing solid content; this trend correlates with the decrease of the loss-tangent/solid-content with increasing solid content.

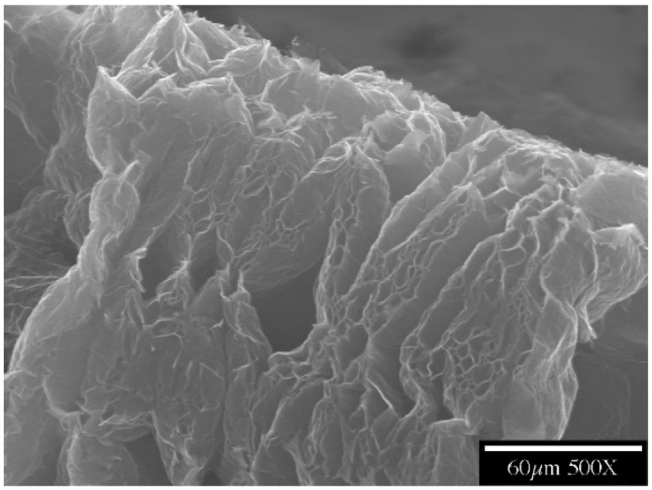

(a)

(b)

(c)

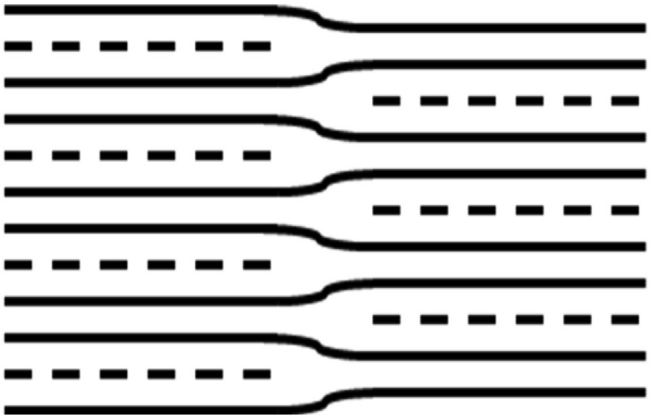

(d)

Fig. 1. (a) SEM photograph of exfoliated graphite. (b) The cellular structure of exfoliated graphite, with each line representing a cell wall and each cell resulting from an intercalate island. (c) The structure of a cell wall, with each line representing a carbon layer (rather than a cell wall). In the case of exfoliated graphite made from sulfuric-acid-intercalated graphite flakes, the cell wall typically consists of about 60 carbon layers. The substantial sliding between adjacent carbon layers necessitates that each carbon layer in the wall of a given cell wall does not extend from one end of the cell wall to the other; as illustrated, the carbon layers in a cell wall are not continuous [9]. (d) The structure of a graphite intercalation compound according to Daumas and Herold [21]. The solid lines indicate the carbon layers. The dashed lines indicate the intercalate layers. The carbon layers are bent at certain locations, thus resulting in intercalate islands between the bend locations. The intercalation compound illustrated here has stage = 2, but the concept applies to any stage [8].

3. Analysis of the previously reported experimental results for exfoliated graphite based on dynamic flexural testing

Experimental results in terms of the loss tangent, storage modulus and loss modulus for exfoliated graphite are shown in Table 1 and have been previously reported [9], using the forced resonance method. The specimen in the form of an exfoliated graphite compact was loaded with a specified static stress together with a sinusoidal stress wave. The resulting static strain and dynamic strain amplitude were measured by using a displacement transducer.

The method entails dynamic flexural testing (three-point bending with a span of 20 mm, with the beam-shaped specimen of length 25 mm, width 8 mm and thickness 3 mm) using a sinusoidal stress wave input at 0.2 Hz (far away from the resonance frequency of the specimen), such that the dynamic stress amplitude is controlled at half of the static stress, with the static stress ranging from 2.5 to 3.8 kPa and the dynamic stress ranging from 1.3 to 1.9 kPa. The resulting static strain is approximately fixed at 2%, with the amplitude of the mid-span deflection variation being below 10 μm.

Analysis of the results of the abovementioned experimental work [9] has not been performed in the prior work for determining the phase angle δ between the input stress wave and the output strain wave, the dynamic strain amplitude ε_0 and the energy loss per unit volume. This section is directed at this analysis.

Please refer to Ref. [9] for the method of material preparation and the structure of the exfoliated graphite. Most importantly, the structure is such that the cell wall consists of about 60 graphite layers (i.e., 20 nm thick for the cell wall) on the average, as indicated by the measured specific surface area of 41 m^2/g for this particular exfoliated graphite [9] and comparing this area with the calculated value for single-layer graphene. Exfoliated graphite compacts of various densities ranging from 0.0236 to 0.3503 g/cm^3 (as determined for each specimen by measuring the weight and dimensions), and hence various values of the solid content ψ (i.e., various solid volume fractions ranging from 1.04% to 15.51%), were prepared by compaction of the exfoliated graphite at various pressures ranging from 0.25 to 7.71 MPa.

A glossary of abbreviations is in Appendix A. The loss tangent ($\tan\delta$) describes the degree of viscous character. The storage modulus E' is the dynamic elastic modulus, which is associated with the stiffness. The loss modulus is the dynamic viscous modulus, which relates to the energy loss per unit volume. In accordance with rheology [26], these quantities are described by the following equations.

$$E' = \frac{\sigma_0}{\varepsilon_0}\cos\delta \tag{1}$$

$$E'' = \frac{\sigma_0}{\varepsilon_0}\sin\delta \tag{2}$$

$$\tan\delta = \frac{E''}{E'} \tag{3}$$

Where σ_0 is dynamic stress amplitude and ε_0 is dynamic strain

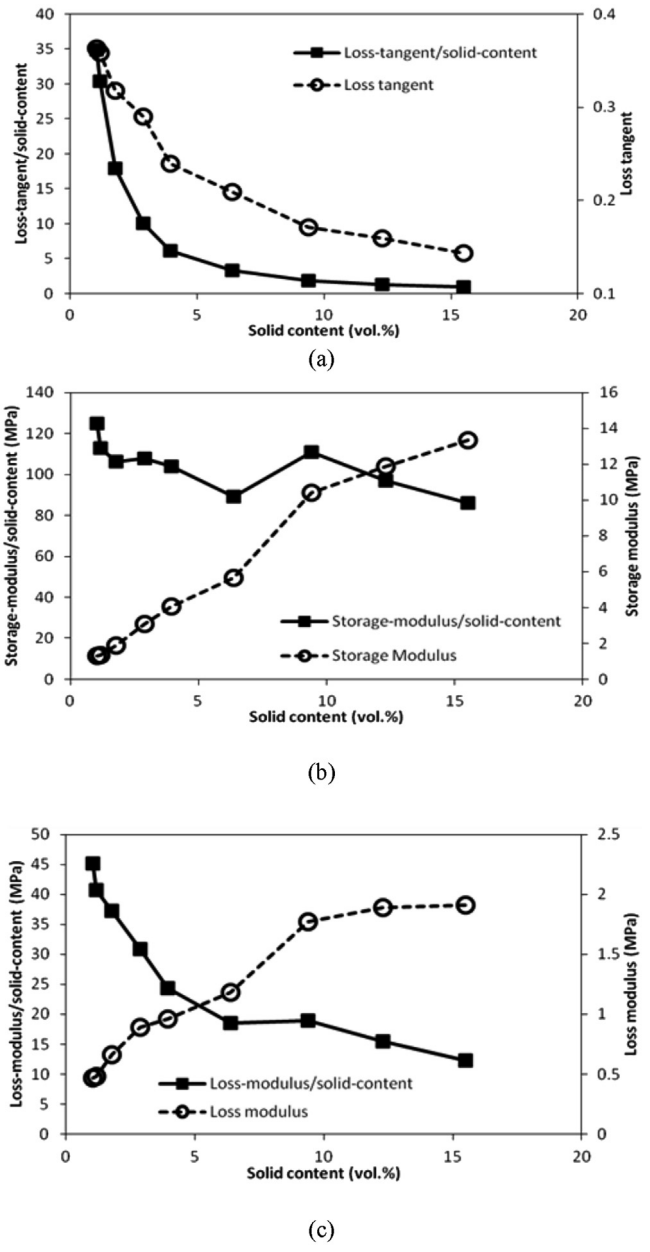

Fig. 2. Dynamic mechanical testing of exfoliated graphite compacts under flexure. (a) Specimen configurations. The dashed parallel lines show the preferred orientation of the graphite layers. (b) Schematic illustrations of the variation of the stress with time during dynamic mechanical testing. The static and dynamic stresses are σ_s and σ_d respectively. (c–e) Dynamic flexural properties at various solid contents, with the static strain at 2% and the frequency at 0.2 Hz [9].

amplitude (Fig. 3(a)).

Based on Eq. (1), the dynamic strain amplitude ε_0 is given by

$$\varepsilon_0 = \sigma_0 \frac{\cos\delta}{E'} \tag{4}$$

Using Eqs. (3) and (4) and the experimental results [9], the values of δ and ε_0 are obtained, as shown in Table 1.

The curve of stress vs. strain in a cycle of loading and unloading that spans positive and negative values of the stress is illustrated in Fig. 3(a) for a viscoelastic material with a nonzero value of δ. The area enclosed by the curves is the energy loss per cycle per unit volume.

The ellipse in Fig. 3(a) can be represented by the equation

$$\left(\frac{\sigma}{\sigma_0}\right)^2 + \left(\frac{\varepsilon}{\varepsilon_0}\right)^2 = (\sin\delta)^2 + 2\left(\frac{\sigma}{\sigma_0}\right)\left(\frac{\varepsilon}{\varepsilon_0}\right)\cos\delta \tag{5}$$

which is the equation of an ellipse with the principle axis inclined to the abscissa by the angle δ. The area of the ellipse is given by Ref. [26], and corresponds to the energy loss E_f per unit volume during a cycle of loading and unloading.

$$E_f = \pi\sigma_0\varepsilon_0\sin\delta \tag{6}$$

Substituting Eq. (2) into Eq. (6) gives

$$E_f = \pi\varepsilon_0^2 E'' \tag{7}$$

Using Eq. (7) and the experimentally determined values of E'', the energy loss E_f per unit volume per cycle is calculated for various solid contents, as shown in Table 1 and Fig. 3(b). The energy loss decreases with increasing solid content. For the same static strain, with the increase of the solid content, there will be more cells per unit volume. As a result, it will be more difficult for the adjacent cell walls to slide with respect to one another. On the one hand, more load will need to be applied in order to force the specimen to bend to the same static strain and this will cause the internal friction force to increase with the solid content. On the other hand, the difficulty of sliding will cause less displacement among the cell walls as the solid content increases. Thus, the energy loss decreases with increasing solid content.

The time-varying stress σ and strain ε with the angular frequency ω (with $\omega = 2\pi f$, where f is the frequency) can be expressed by the following equations. Furthermore, if plotting the strain and stress with the corresponding sinusoidal function as Eq. (8) and Eq. (9), the loss energy per unit volume can be verified from the calculation of the close ellipse area in another way.

$$\sigma = \sigma_s + \sigma_0\sin(\omega t) \tag{8}$$

$$\varepsilon = \varepsilon_s + \varepsilon_0\sin(\omega t - \delta), \tag{9}$$

where σ_s and ε_s are the static stress and static strain respectively, and σ_0 and ε_0 are the magnitudes of the dynamic stress and dynamic strain respectively. The strain wave lags the stress wave by the phase angle δ. The plot of stress vs. strain in a cycle, as obtained using Eq. (8) and Eq. (9), is shown in Fig. 3(c) for each value of the solid content and the corresponding static strain ε_s.

Numerical computing using the programming language MATLAB gives the area of each ellipse in Fig. 3(c) and hence the energy loss per cycle per unit volume, as shown in Table 1. The values of the energy loss thus obtained are close to those obtained using Eq. (7). The consistency confirms the validity of the experimental results.

4. Model of interfacial-friction-based viscoelastic behavior

4.1. Basic concept in the interfacial viscoelastic model

The model developed in this work is hereby referred to as the Interfacial Viscoelastic Model (IVM). The classical equation that embodies the mechanics of three-point bending assumes purely elastic behavior. Thus, let us assume for the sake of argument that the material is regarded purely as elastic one. The classical equation is

$$\Delta z = \frac{\varepsilon L_s^2}{6H} \tag{10}$$

where Δz is the mid-span deflection, L_s is the span, ε is the strain and H is the thickness of the beam.

Table 1
Values of the phase angle δ, the dynamic strain amplitude ε_0, the energy loss E_f per unit volume per cycle (based on rheology), the mid-span deflection (calculated static value Δz_s, calculated dynamic value Δz_0 and the measured dynamic value Δz), the load (static load P_s, maximum dynamic load P_{max} and minimum dynamic load P_{min}), the magnitude of the equivalent friction force F_{max}, the number N of cell layers, and the equivalent sliding displacement S_e, the energy loss W_f per unit volume per cycle (based on the friction-based viscous model of this work) and the error of W_f relative to E_f for exfoliated graphite compacts of various solid contents ψ and various densities ρ, and with various pore sizes D. Please refer to Table 1 of Ref. [9] for the data scatter range for the experimentally determined quantities, i.e., ψ, ρ, tan δ, E' and E''.

ψ (%)		1.04	1.18	1.77	2.88	3.94	6.38	9.40	12.30	15.51
ρ (g/cm^3)		0.0236	0.0267	0.0401	0.0650	0.0891	0.1442	0.2124	0.2780	0.3503
D (μm)		1.36	1.20	0.796	0.486	0.351	0.211	0.139	0.103	0.078
Stress (Pa)	σ_s	2540	2580	2680	2760	2880	3020	3260	3480	3760
	σ_0	1270	1290	1340	1380	1440	1510	1630	1740	1880
ε_s (%)		2.1	2.1	1.9	2.0	2.0	2.1	2.2	2.0	2.1
$tan\ \delta$		0.363	0.358	0.318	0.290	0.239	0.209	0.171	0.159	0.143
E' (MPa)		1.30	1.36	2.09	3.10	4.08	5.66	10.40	11.90	13.34
E''(MPa)		0.47	0.48	0.66	0.89	0.96	1.18	1.77	1.89	1.91
ε_0 (10^{-4})		9.183	9.132	6.110	4.275	3.433	2.611	1.545	1.444	1.395
δ (°)		39.90	39.40	35.28	32.34	26.88	23.61	19.41	18.07	16.28
E_f (J/m^3)	Eq. (7)	1.245	1.258	0.774	0.511	0.355	0.253	0.133	0.124	0.117
	Fig. 5	1.247	1.244	0.777	0.515	0.360	0.253	0.133	0.124	0.116
Mid-span deflection (μm)	Δz_s	466.7	466.7	422.2	444.4	444.4	466.7	488.9	444.4	466.7
	Δz_0	40.82	40.58	27.16	19.00	15.26	11.60	6.86	6.42	6.20
	Δz	8.80	8.90	8.60	8.70	6.00	7.00	6.50	6.30	6.10
Mass M (mg)		14.2	16.0	24.1	39.0	53.5	86.5	127.4	166.8	210.2
Load (mN)	P_s	6.1	6.2	6.4	6.6	6.9	7.2	7.8	8.4	9.0
	P_{max}	9.1	9.3	9.6	9.9	10.4	10.9	11.7	12.5	13.5
	P_{min}	3.0	3.1	3.2	3.3	3.5	3.6	3.9	4.2	4.5
F_{max} (mN)		0.1077	0.1241	0.1713	0.2630	0.3116	0.4718	0.6170	0.8057	0.9918
$\Delta\varepsilon_h$ ($10^{-4}\varepsilon$)						0.1334				
$\Delta\varepsilon_D$ ($10^{-4}\varepsilon$)		9.090	8.024	5.310	3.240	2.338	1.408	0.924	0.684	0.522
N		1560	1770	2655	4320	5910	9570	14100	18450	23270
S_e (mm)		7.015	6.166	2.747	1.186	0.695	0.326	0.131	0.094	0.072
W_f (J/m^3)	Eq. (36), Fig. 8	1.242	1.258	0.773	0.512	0.356	0.253	0.133	0.124	0.117
Error (%) of W_f vs. E_f (Eq. (7))		−0.336	−0.033	−0.174	0.192	−0.012	0.045	0.084	0.326	0.247

With the strain being time-varying, the maximum and minimum values of Δz in a cycle are given respectively by

$$\Delta z_{max} = \frac{\varepsilon_{max} L_s^2}{6H} = \frac{(\varepsilon_s + \varepsilon_0) L_s^2}{6H} \tag{11}$$

$$\Delta z_{min} = \frac{\varepsilon_{min} L_s^2}{6H} = \frac{(\varepsilon_s - \varepsilon_0) L_s^2}{6H} \tag{12}$$

Hence, the dynamic amplitude of Δz is given by the difference between the maximum and minimum values, i.e.

$$\Delta z_0 = \Delta z_{max} - \Delta z_{min} = \frac{\varepsilon_0 L_s^2}{3H} \tag{13}$$

By using the static strain and dynamic strain in the experimental results, the values of the dynamic value Δz_0 and the static value Δz_s are calculated, as shown in Table 1. The calculated dynamic value is close to the measured dynamic value Δz for three highest values of the solid content, but is greater than the measured value for all the other values of the solid content, as shown in both Table 1 and Fig. 3(d). The lower is the solid content, the more the calculated value exceeds the measured value. This reflects the primarily elastic character of the specimens with the three highest values of the solid content and the increasing viscous character as the solid content decreases. The calculation based on Eq. (10) assumes purely elastic behavior, so consistency between the calculated and measured values occurs only at the high values of the solid content. This means that a viscoelastic material will becomes greater in its elastic character as the solid content increases.

With a broad view of materials in general, a pure elastic material may be regarded as a special kind of viscoelastic material. It is well known that a viscoelastic material can be modeled as a spring (the elastic component) and a dashpot (the viscous component) in parallel. If the dashpot is absent, the material is purely elastic. The greater is the dashpot contribution, the stronger is the viscous character. For exfoliated graphite, the higher is the solid content, the greater is the spring contribution; the lower is the solid content, the greater is the dashpot contribution. If a combination of a spring and a dashpot is represented by a series of micro-springs and micro-dashpots, the elastic and viscoelastic behavior can be described in terms of the following model. A purely elastic material is hereby modeled as multiple layers of micro-springs that are in series within each layer (Fig. 4(a)). The various micro-springs function independently as the beam is bent. The magnitude of the flexural strain for each layer, as indicated by arrows in Fig. 4(a), increases linearly with increasing distance of the layer from the central plane.

For a viscoelastic material, the model in Fig. 4(a) is adjusted by the addition of micro-dashpots, so that each micro-spring is replaced by a Voigt element. Thus, the microstructure of exfoliated graphite shown in Fig. 1(c) is described as a series of interconnected Voigt elements illustrated in Fig. 4(b).

In the IVM model, the flexural stress and strain are assumed to vary linearly as a function of the distance from the central plane, but the interconnected Voigt elements of adjacent layers are dependent on each other. At the extremity of a cell in exfoliated graphite, two cell walls merge and they can slide relative to one another. This sliding is enabled by the fact that a cell wall in the extremity region is a part of the overall cell wall and the fact that the cell walls in different layers experience different strains due to their difference in position relative to the central plane.

4.2. Assessment of the friction force

The friction force is a resistance to absorb or counteract the energy applied by the load. Values of the friction coefficient are not available for the interfaces between graphite layers, so it is not possible to calculate the friction force based on the friction

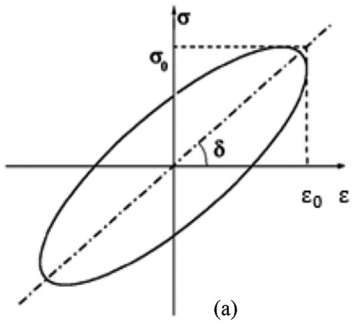

(a)

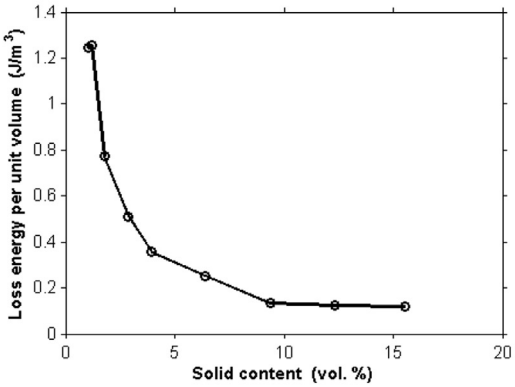

(b)

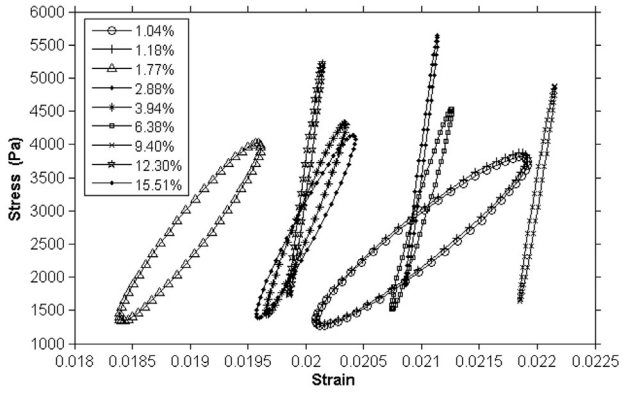

(c)

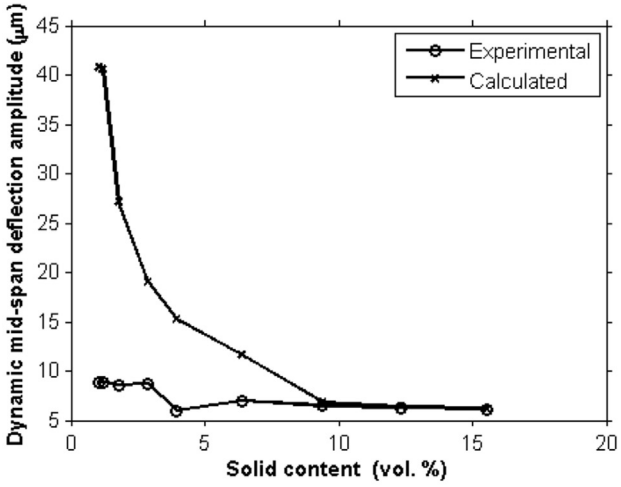

(d)

coefficient and normal force (here is the load applied on the beam). But the analysis of the friction force involves firstly the evaluation of the load, which is useful for assessing the approximate range of the friction force. The magnitude of the load and that of the friction force should be at the same level and the variation trend of both forces with respect to solid content should be similar.

The specimen mass, as calculated from the density and volume, is very small, as shown in Table 1. Thus, the load is expected to be small.

If the specimen is an elastic beam in three-point flexure testing, the load P has the following relationship with the stress σ,

$$P = \frac{2BH^2\sigma}{3L_s} \tag{14}$$

where B and H are the width and thickness respectively. If the dynamic stress is a sinusoidal wave as expressed by Eq. (8), the dynamic load to force the specimen to bend will satisfy the equation

$$P = \frac{2BH^2[\sigma_s + \sigma_0 \sin(\omega t)]}{3L_s} \tag{15}$$

Using Eq. (15), which assumes elasticity, the static load P_s, the maximum dynamic load P_{max} and the minimum dynamic load P_{min} are calculated for the various values of the solid content, as shown in Table 1. Thus, the load is of the order of mN and increases with increasing solid content. This means that the friction force has the same order of magnitude and the same trend with respect to the solid content.

Based on the conventional friction theory, the friction force is given by the product of the normal pressure and the friction coefficient. The load mentioned above is calculated based on the assumption of elasticity, so its values cannot be used for calculation of the friction force of viscoelasticity. Therefore, a different concept to assess the friction force involving viscoelastic theory is needed.

As mentioned in Section 4.1, the stress in a Voigt element includes two parts that correspond to a spring and a dashpot, i.e.,

$$\sigma = E_s\varepsilon + \eta_s\dot{\varepsilon} \tag{16}$$

where E_s is the elastic modulus for a spring, and η_s is the viscosity for the dashpot in the equivalent mechanical model consisting of a spring and a dashpot in parallel. The equivalent friction force can be calculated from the second term on the right side of Eq. (16), and the viscosity η_s is related to loss modulus E'' by the equation (17).

$$\eta_s = \frac{E''}{\omega} = \frac{E''}{2\pi f} \tag{17}$$

For the sinusoidal load described by Eq. (9), the equivalent friction force F can be expressed as shown in Eq. (18), where the solid content ψ is introduced because the porous nature of the material will obviously affect the internal friction and the friction force will be less than that of the corresponding non-porous material. Substituting η_s from Eq. (17) and use of Eq. (9) give the relationship between F and E'', i.e.

Fig. 3. Analysis based on conventional rheology. (a) Graphical representation of the stress-strain relationship of a viscoelastic material with a non-zero value of δ. (b) The energy loss per unit volume per cycle vs. the solid content. (c) The strain-stress curve in a cycle for different solid contents. (d) Dynamic mid-span deflection amplitude (both calculated and measured values) vs. the solid content.

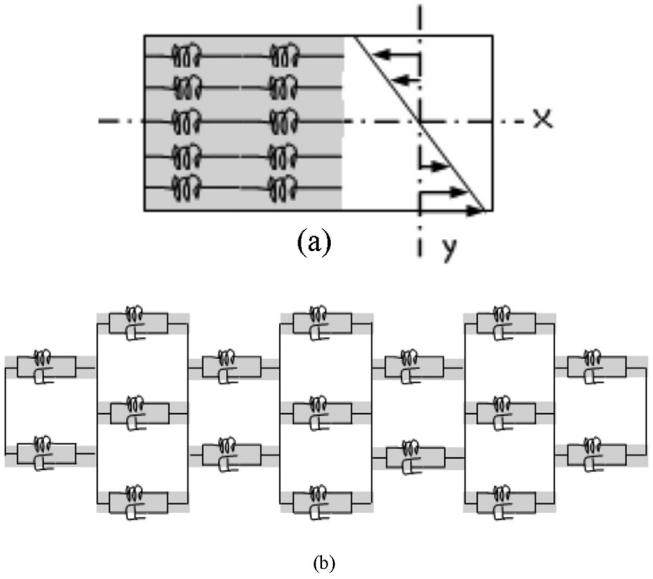

Fig. 4. Mechanical models of materials. (a) A purely elastic material modeled as multiple equivalent micro-springs arranged in layers, with all the springs exhibiting the same purely elastic stress-strain behavior. (b) A viscoelastic materials modeled as interconnected layers of Voigt elements, which represent the cell walls. Each pore in a cell of exfoliated graphite is encased by cell walls. This is the framework of the Interfacial Viscoelastic Model (IVM) of this work.

$$F = \eta_s \dot{\varepsilon} A\psi = \eta_s \omega A\psi \varepsilon_0 \cos(\omega t - \delta) = E'' \varepsilon_0 BH\psi \cos(\omega t - \delta) \tag{18}$$

where A is the cross-section area, which is equal to BH, where H is the thickness and B is the width of the specimen.

Eq. (18) shows that, during loading and unloading, the friction force (a vector) changes direction and follows the load with the delay by the phase angle δ as well. The friction force is in phase with the strain (Eq. (9)), so the phase angle δ can be omitted from Eq. (18). Thus, the equivalent friction force F_e is given by

$$F_e = \eta_s \dot{\varepsilon} A\psi = E'' \varepsilon_0 BH\psi \cos(\omega t) \tag{19}$$

It is noted that F_e is delayed relative to the load by the phase angle δ. Using Eq. (19) and the experimental results, the amplitude of F_e is calculated, as shown in Table 1. These values are in the unit mN, as for the load values, and their trend with respect to the solid content is the same as that for the load. Fig. 5 shows the dependence of both quantities on the solid content.

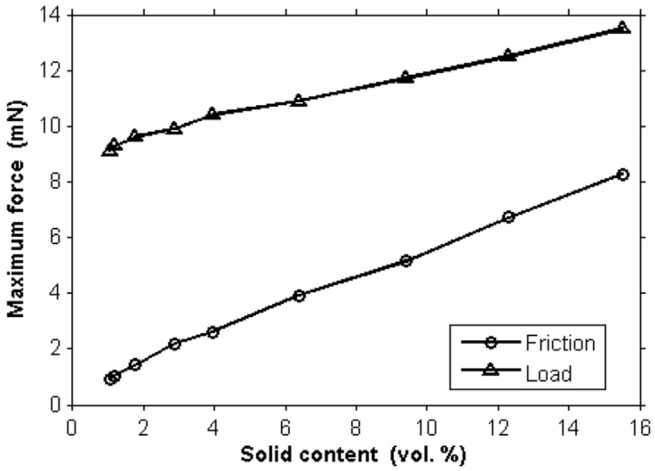

Fig. 5. Dependence of the maximum load and the friction force on the solid content.

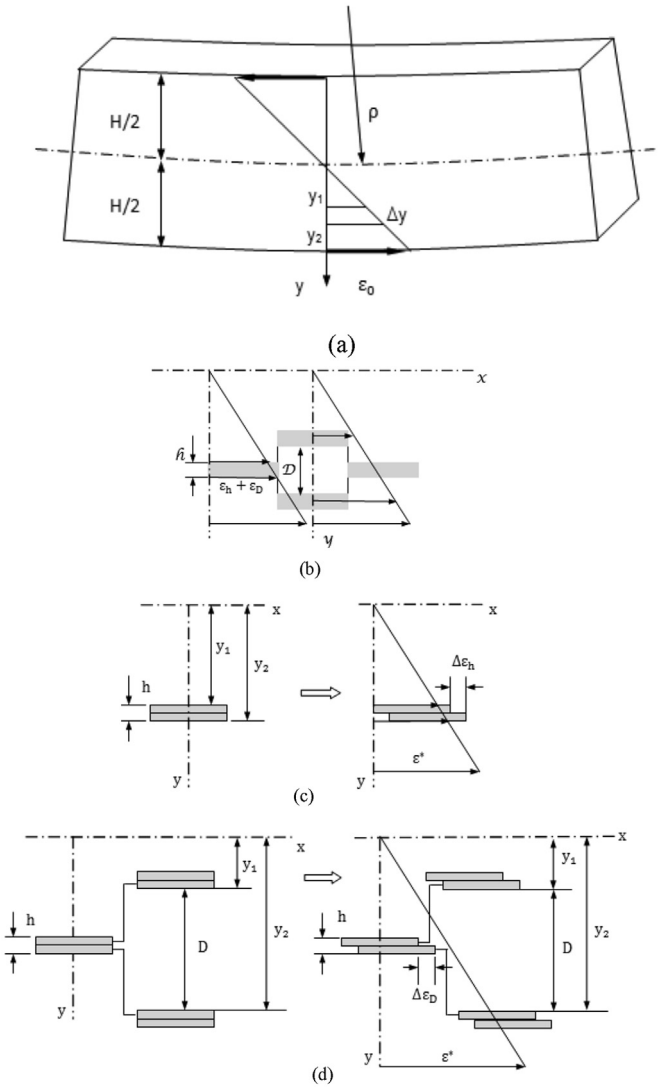

Fig. 6. Illustration of the origins of the displacement upon flexure. (a) The flexural strain (indicated by horizontal arrows) of an elastic beam is determined by the position relative to the central plane (dashed line) and the bending moment. (b) A pore surrounded by four cell walls, which are the four blocks (four shaded areas). The differential strain of a cell wall is affected by the cell wall thickness and the longitudinal compression or tension of the adjacent connected cell walls. (c) Displacement due to the differential strain within a cell wall. An interface within a cell wall of thickness h slides during flexure of the beam due to this differential strain. Left panel: Before sliding. Right panel: After sliding. (d) Displacement due to the differential strain between interconnected cell walls. The interface between the merged cell walls at the cell extremity undergoes sliding during flexure. Left panel: Before sliding. Right panel: After sliding.

4.3. Assessment of the sliding displacement

For an elastic beam, the flexural strain at the central plane is zero, as illustrated in Fig. 6(a). The upper part of the beam is under longitudinal compressive and the lower part of the beam is under longitudinal tension.

For the case of pure flexure, if the flexural radius is ρ, then the flexural strain ε at position y in the beam is given by

$$\varepsilon = \frac{y}{\rho}\ , \tag{20}$$

where y is distance from the central plane, as illustrated in Fig. 5(a). Thus, the maximum flexural strain ε^* is at the farthest position away from the central plane ($y = H/2$, where H is the thickness of the beam) and can be measured by using an attached strain gage at the central outer surface of the beam. Hence,

$$\varepsilon^* = \frac{H}{2\rho}\ . \tag{21}$$

Therefore, a slab of incremental thickness Δy within the beam will have the differential strain $\Delta\varepsilon$ across its thickness

$$\Delta\varepsilon = \frac{y_2 - y_1}{\rho} = \frac{\Delta y}{\rho} = \frac{2\Delta y}{H}\varepsilon^*. \tag{22}$$

Consider the cellular structure illustrated in Fig. 1(c). The cell wall consists of about 60 graphite layers, as illustrated in Fig. 1(d). Let the cell size (i.e., pore size) in the vertical direction of Fig. 1(c) be D. Let the thickness of the cell wall be h (20 nm in this case). Upon tension in the horizontal direction of Fig. 1(c), D decreases and the cell wall is stretched; upon compression in this direction, D increases and the cell wall is shortened.

Due to the small thickness of a cell wall, the differential displacement between adjacent layers in a cell wall is small. However, adjacent cell walls meet at the extremities of a cell, as illustrated in Fig. 1(c). Although the sliding between the adjacent cell walls occurs at the cell extremities, the sliding involves participation of the entirety of each cell wall, including the parts of the cell wall away from the cell extremities.

Fig. 6(b) illustrates cell walls (each with thickness h) around a pore (with height D). This corresponds to a part of the cellular structure of Fig. 1(c) and is a basic component in the IVM model. The cell walls around a pore can be simply considered as four blocks (the four shaded areas in Fig. 6(b)) that are positioned in three layers, with two blocks located in the middle layer and the other two blocks located in the two layers above and below the middle layer. Each block is a micro Voigt element. The connection of the blocks of adjacent layers enables more sliding displacement than what each block, based on its own thickness, can contribute.

The beam has thickness H (Fig. 6(a)). The horizontal dashed line indicates the neutral axis during flexure. With the assumption that the stress and strain in each layer are linearly related to the distance from the neutral axis, the differential strain $\Delta\varepsilon_h$ of a block across its own thickness h is given by

$$\Delta\varepsilon_h = \frac{2h}{H}\varepsilon^* \tag{23}$$

Fig. 6(c) illustrates the displacement associated with this differential strain.

In case of exfoliated graphite, the blocks (cell walls) are interconnected, as illustrated in Fig. 6(d). The differential strain $\Delta\varepsilon_D$ associated with the sliding between the connected blocks that sandwich a pore with pore size D is

$$\Delta\varepsilon_D = \frac{2D}{H}\varepsilon^*. \tag{24}$$

Because D is much larger than h, $\Delta\varepsilon_D$ is much larger than $\Delta\varepsilon_h$ (Eq. (23)). The total differential strain $\Delta\varepsilon$ of a cell wall (a block) is the sum of $\Delta\varepsilon_D$ and $\Delta\varepsilon_h$, with the latter being negligible. Hence,

$$\Delta\varepsilon = \Delta\varepsilon_D + \Delta\varepsilon_h = \frac{2(D+h)}{H}\varepsilon^* \approx \frac{2D}{H}\varepsilon^* \tag{25}$$

Based on the theory of Johnson, Koplik and Schwartz (JKS) [27], D is given by

$$D = \frac{2}{\beta\frac{S_p}{V_p}} \tag{26}$$

where β is a dimensionless constant that is generally set at 1.5, and V_p and S_p are the volume and surface area of all the pores in the specimen respectively, with

$$S_p = V\rho A_p = LBH\rho A_p \tag{27}$$

$$V_p = V(1-\psi) = LBH(1-\psi) \tag{28}$$

where L, B and H are the length, width and thickness of the specimen respectively, ρ is the density, $V = LBH$ is volume of the specimen, A_p is the specific surface area per unit mass (assuming that all the pores are open pores), and ψ is the solid content.

The sliding displacement Δs between adjacent cell walls is thus given by

$$\Delta s = \frac{2DL}{H}\,\varepsilon^* \tag{29}$$

Let $\varepsilon^* = \varepsilon_s + \varepsilon_0 \sin(\omega t)$ in order to introduce the time dependence of the dynamic strain. During a cycle, which includes a loading and unloading segments, the sliding displacement of a cell wall for all segments should be evaluated by integration. However, if Eq. (29) is integrated with respect to time from 0 to T, where T is the period of a cycle, the result is zero. This is because the displacement is a vector.

$$S_c = \int_0^T \frac{2DL}{H}[\varepsilon_s + \varepsilon_0 \sin(\omega t)]dt \tag{30}$$

For frictional sliding, the displacement in both directions should be considered. Thus, the total sliding displacement S_c in a cycle with respect to a cell wall is given by doubling the value obtained by the integration from 0 to $T/2$.

$$S_c = 4\int_0^{T/2} \frac{DL}{H}[\varepsilon_s + \varepsilon_0 \sin(\omega t)]dt \tag{31}$$

The total sliding displacement is the sum of the displacement of all the cell walls in the beam. For the sake of simplicity, the number N of cell walls in the specimen is given by

$$N = \psi\frac{H}{h} \tag{32}$$

The values of N for various solid contents are shown in Table 1. The equivalent sliding displacement S_e of the totality of all the cell walls is a function of time t, which is given by

$$S_e = 4\lambda N\Delta s = \frac{8\lambda DL\psi}{h}[\varepsilon_s + \varepsilon_0 \sin(\omega t)] \tag{33}$$

where λ is a coefficient that describes the deformation of the viscoelastic beam during flexure, as explained below.

In the theory of elasticity, the Poisson's ratio is used to describe the transverse dimensional change upon longitudinal deformation. For a viscous material, when the specimen is stretched in the length direction, the width and thickness change as well, and such non-axial dimensional changes will also affect the sliding displacement. Thus, a deformation factor λ is introduced. It is a dimensionless coefficient that describes the extent of off-axis dimensional

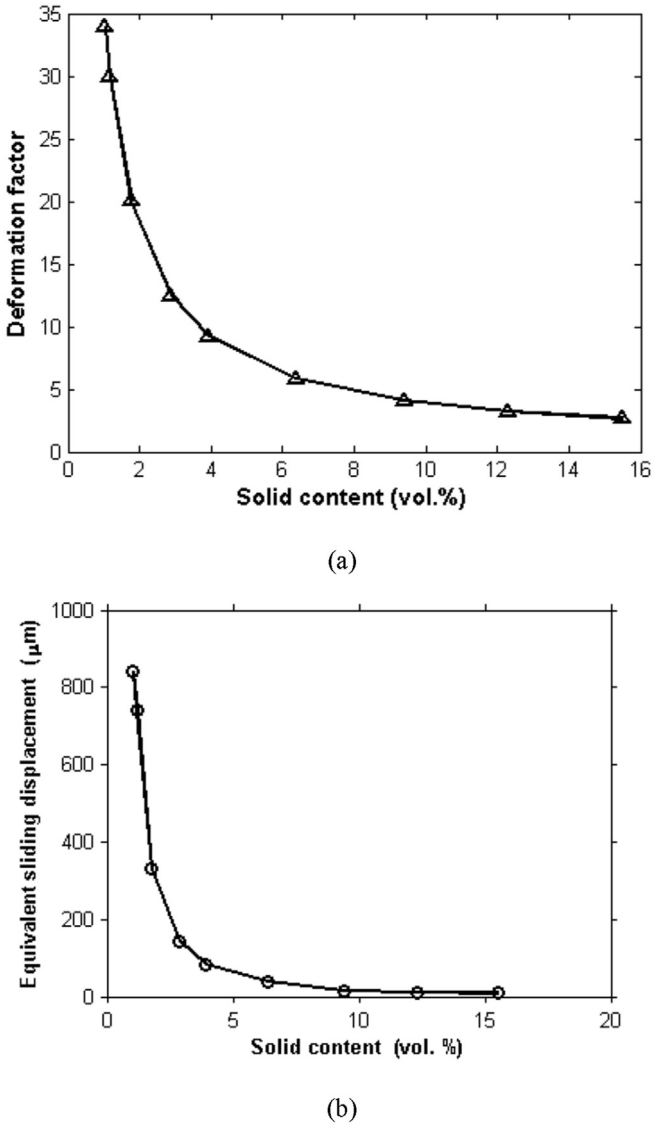

Fig. 7. Parameters in the interfacial-friction-based model of viscous behavior. (a) Deformation factor λ vs. the solid content. (b) The equivalent sliding displacement Se vs. the solid content.

change upon viscous deformation under an axial applied stress and is defined in this work as

$$\lambda = \frac{kB}{L\psi(1-\psi)} \tag{34}$$

This factor reflects the effects of the width B and length L, and the solid content ψ. The quantity k is a dimensionless adjustable factor that is close to 0.5. The term $1-\psi$ describes the pore content. Both the solid content and the pore content affect the viscoelastic behavior. Eq. (34) means that λ as a function of ψ is symmetric around $\psi = 0.5$. In the case of exfoliated graphite compacts, the regime $\psi < 0.5$ is relevant. Fig. 7(a) shows the decrease of λ with increasing ψ in the case of exfoliated graphite compacts. The higher is λ, the more is the extent of viscous character. This trend is consistent with Fig. 3(d), which shows that the viscous character increases with decreasing ψ, so that the experimental curve increasingly deviates from the curve calculated by assuming purely elastic behavior. Moreover, when ψ exceeds 0.1, the experimental and calculated curves overlap, indicating mainly elastic behavior.

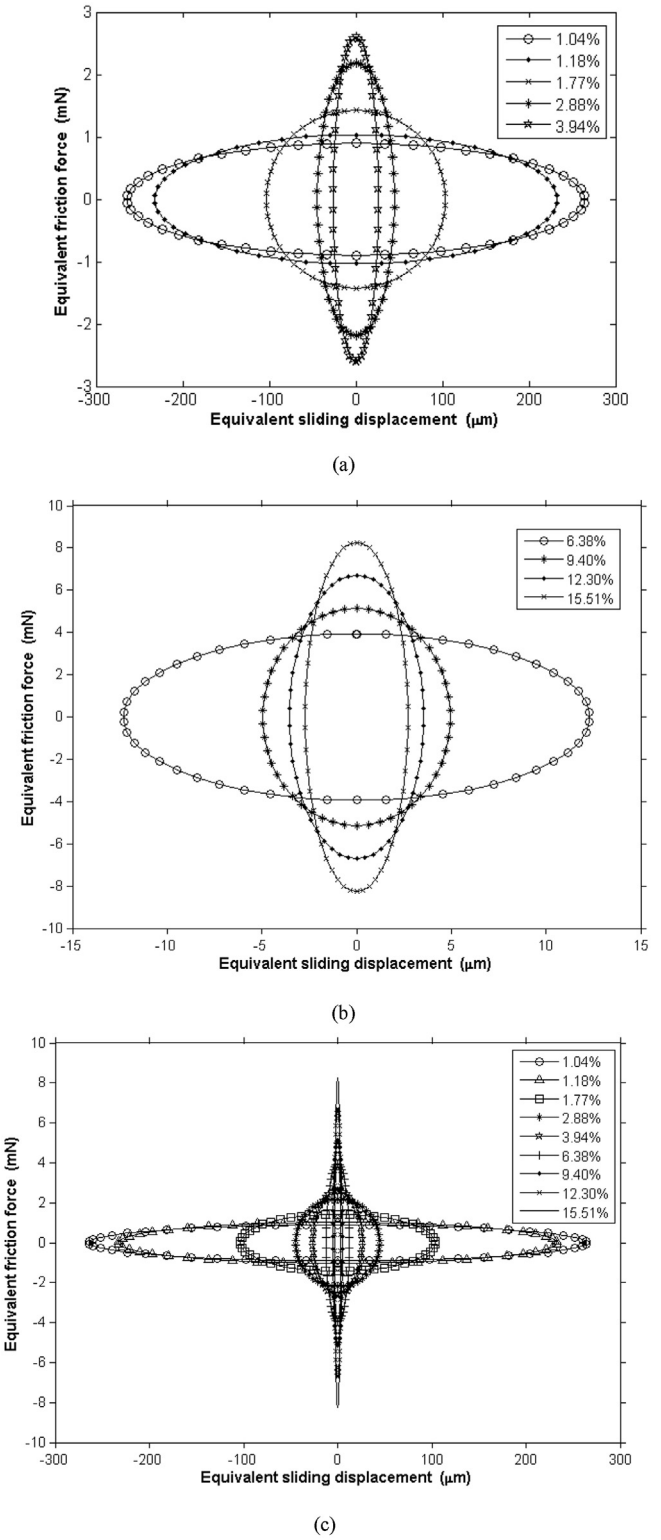

Fig. 8. Energy loss per unit volume per cycle for different solid contents, as obtained from the interfacial-friction-based model of viscous behavior. (a) Solid content (1.04–3.94 vol%). (b) Solid content (6.38–15.51 vol%). (c) Solid content (1.04–15.51 vol%).

The total displacement in a loading-unloading cycle of period T is the sum of the sliding distances for all the cell walls in the period. Since there are four segments of loading and unloading in a cycle (starting at strain = 0), the total displacement S_T in a cycle of period T is given by

$$S_T = 4\lambda NS_c = 2\int_0^{T/2} S_e dt = 2\int_0^{T/2} \frac{8\lambda DL\psi}{h[\varepsilon_s + \varepsilon_0 \sin(\omega t)]dt} \quad (35)$$

For frequency $f = 0.2$ Hz and $k = 0.545$, Eq. (35) gives the total equivalent sliding displacement S_T in the specimen; the values are shown in Table 1 and Fig. 7(b). The S_T value decreases with increasing solid content. This trend is because of the increasing difficulty of sliding as the solid content increases. In spite of the increase in the load as the solid content increases (Table 1), the friction increases.

4.4. Assessment of the energy dissipation

Specimens of different solid contents produce different amounts of energy dissipation, as caused by friction. In a cycle of loading and unloading, the equivalent friction force and equivalent sliding displacement are all dependent on time t, so the energy dissipation is also a function of time t. The dissipation is given by the product of the equivalent friction force and the equivalent sliding displacement. It is noted that there is no phase angle between the friction force and the sliding displacement. According to Eq. (19) and Eq. (33), the energy is not a vector quantity, since the product of the friction force and the sliding displacement is positive at any time in a cycle. Therefore, the energy loss W_f per unit volume in a cycle of period T is given by

$$\begin{aligned} W_f &= \frac{\int_0^T F_e S_e dt}{V} = \frac{\int_0^T F_e S_e dt}{LBH} \\ &= \int_0^T \frac{8kBD\psi}{Lh(1-\psi)} E'' \varepsilon_0[\varepsilon_s + \varepsilon_0 \sin(\omega t)]\cos(\omega t)dt \\ &= \int_0^T \frac{8kBD\psi}{Lh(1-\psi)} E'' \varepsilon_0^2 \sin(\omega t)\cos(\omega t)dt \\ &= \int_0^T \frac{4kBD\psi}{Lh(1-\psi)} E'' \varepsilon_0^2 \sin(2\omega t)dt \end{aligned} \quad (36)$$

To evaluate the above integration function, the programming language MATLAB has been written. This involves evaluating the equivalent friction force and the equivalent sliding displacement separately, and then using trapezoidal numerical integration trapz() to evaluate the area of the closed ellipse. The code is shown in Appendix B.

The W_f is calculated for various values of coefficient k. It is thus found that the value $k = 0.545$ gives the best fit between W_f (based on Eq. (36), i.e., the friction-based model) and E_f (based on Eq. (7), i.e., rheology).

Fig. 8 shows the elliptical curve of friction force vs. displacement (with the included area being the energy loss per unit volume per cycle) for different solid contents, as calculated for $k = 0.545$. The greater is the solid content, the smaller is the displacement, the higher is the friction force, the less is the energy loss and the lower is the degree of viscous character.

4.5. Implication to the elastomeric strain

Based on the notion of the displacement of the graphite layers relative to one another within a cell wall of exfoliated graphite during deformation, the instrumented indentation results were interpreted to give a reversible engineering shear strain of up to 35 (3500%) for the cell wall [11]. This work shows that the displacement is between the cell walls rather than between the graphite layers in a cell wall. Therefore, the shear strain previously reported for a solid content of 4 vol% was much overestimated. During instrumented indentation, it is unclear how many cell walls are involved in the deformation. If two cell walls are involved, with the pore size D between them being 0.351 μm (calculated based on Eq. (26) for the solid content of 4 vol%), the shear strain would be 2.0 (200%). This value is the upper bound, since the value will be smaller if more than two cell walls are involved in the indentation deformation.

5. Conclusion

The viscous behavior of solids is valuable for vibration damping and sound absorption. This paper provides an interfacial-friction-based analytical model for solid-state viscous behavior. This model is in contrast to the conventional bulk viscous deformation model. Exfoliated graphite has been previously shown experimentally to be highly viscous due to the interfacial-friction-based mechanism of energy dissipation [9,10], though the scientific origin has not been previously clarified.

The analytical model of this work is applied to exfoliated graphite compacts with various solid contents. The model is constructed to calculate the interfacial-friction-based energy loss by consideration of the equivalent friction force and the equivalent sliding displacement. These quantities are in phase, varying with time during dynamic sinusoidal loading. Each cell in the exfoliated graphite is modeled as a pore bounded by cell walls, such that the extremities of the adjacent cells at different positions along the height of the specimen beam (under dynamic flexure) meet. A cell wall is modeled as a series of micro Voigt elements. A dimensionless deformation factor λ is introduced to describe the extent of off-axis dimensional change upon viscous deformation under an axial applied stress. Excellent agreement has been obtained between the modeling results and previously reported low-amplitude dynamic flexural experimental results (in terms of the loss tangent and loss modulus at a fixed frequency).

The viscous behavior of exfoliated graphite is found to stem primarily from the sliding between the cell walls that have merged in order to form the cellular structure. The contribution of the sliding between the graphite layers within a cell wall is negligible, due to the small displacement between these layers. The greater is the solid content, the smaller is the displacement, the higher is the friction force, the less is the energy loss and the lower is the degree of viscous character.

This paper is significant in that it establishes the interfacial-friction-based viscous behavior in exfoliated graphite. The concept behind the model presented in this paper may be applied to various solid materials (e.g., nanotube compacts [28]) with an abundance of interfaces at which a degree of sliding is possible.

Acknowledgements

The authors are grateful to Professors K.H. Jiang, C.P. Jiang, S.Z Li and G. Zhao of Beihang University for stimulating discussion. They also thank Mr. J.B. Peng and Miss F.Y. Liu of Beihang University for technical assistance. The financial support of China Scholarship Council (No.201303070208) for the first author is also acknowledged.

Appendix A

Glossary of abbreviations

A	Cross-sectional area of the specimen beam of thickness H and width B
A_p	Specific surface area of the exfoliated graphite
B	Width of the specimen
D	Pore size of the cell in the exfoliated graphite specimen
E_s	Elastic modulus of a spring
$E^{'}$	Storage modulus
$E^{''}$	Loss modulus
E_f	Loss energy per unit volume per cycle based on the rheological theory
F	Interfacial friction force
F_{max}	Maximum interfacial friction force
F_e	Equivalent interfacial friction force
f	Frequency of the sinusoidal wave
H	Thickness of the specimen beam
h	Thickness of a cell wall
k	Dimensionless constant in deformation factor
L	Length of the specimen
L_s	Span distance in dynamic flexure testing
M	Mass of the specimen
N	Number of cell walls in the specimen
P	Force of the load
P_s	Force of the load with respect to the static strain given by the three-point flexure theory
P_{max}	Maximum force of the load given by three-point flexure theory
P_{min}	Minimum force of the load given by three-point flexure theory
S_p	Surface area of all the pores in the specimen
S_c	Equivalent sliding displacement between any adjacent cell walls per cycle
S_e	Total equivalent sliding displacement of all the cell walls in the specimen at time t
S_T	Total equivalent sliding displacement for all the cell walls in the specimen per cycle
Δs	Sliding displacement between any adjacent cell walls corresponding to the strain
T	Period of a cycle including loading and unloading
t	Time variable
V	Volume of the specimen
V_p	Volume of all the pores in the specimen
W_f	Equivalent work done or equivalent energy dissipation by internal friction per unit volume per cycle
Δz	Mid-span deflection measured in dynamic flexural testing
Δz_s	Mid-span deflection corresponding to the static strain given by three-point flexure theory
Δz_0	Mid-span deflection corresponding to the dynamic strain given by three-point flexure theory
Δz_{max}	Maximum mid-span deflection given by three-point flexure theory
Δz_{min}	Minimum mid-span deflection given by three-point flexure theory
β	Dimensionless constant in the pore size evaluation formula given by JKS
δ	Phase angle between the stress and the strain in dynamic flexure testing
ε	Strain variable
ε_s	Static strain
ε_0	Amplitude of the dynamic strain
ε_{max}	Maximum strain during dynamic flexural testing
ε_{min}	Minimum strain during dynamic flexural testing
$\Delta\varepsilon$	Differential strain between the top and bottom of a block in the interfacial-friction-based model
$\Delta\varepsilon_h$	Differential strain of a cell wall
$\Delta\varepsilon_D$	Differential strain caused by a pore
ε^*	Strain at the bottom of the beam
$\dot{\varepsilon}$	Derivative of the strain with respect to time, representing the strain change rate
η_s	Viscosity of a dashpot component
ρ	Density
λ	Deformation factor
σ	Stress variable
σ_s	Static stress
σ_0	Dynamic stress
ψ	Solid content (i.e., solid volume fraction) of exfoliated graphite
ω	Angular frequency

Appendix B

MATLAB code

```
LossModulus = 1e6 * [0.47 0.48 0.66 0.89 0.96 1.18 1.77 1.89 1.91];
StaticStrain = [0.0210 0.0210 0.0190 0.0200 0.0200 0.0210 0.0220 0.0200 0.0210];
DynamicStrain = 1.0e−003 * [0.9183 0.9132 0.6110 0.4275 0.3433 0.2611 0.1545 0.1444 0.1395];
PoreDiameter = 1e−6 * [1.3636 1.2036 0.7966 0.4859 0.3506 0.2111 0.1387 0.1026 0.0784];
SolidContent = [1.04 1.18 1.77 2.88 3.94 6.38 9.40 12.30 15.51]/100;
L = 25*1e−3; B = 8*1e−3; H = 3*1e−3; h = 20*1e−9; freq = 0.2;
RadFreq = 2*pi()*freq;
Volume = L*B*H;
T = [0:0.1:5];
k = 0.545; i = 1;
FK = LossModulus(i)*DynamicStrain(i)*H*B*SolidContent(i)*cos(RadFreq*T);
SK = 8*k*PoreDiameter(i)* B/(h*(1-SolidContent(i)))*(StaticStrain(i) + DynamicStrain(i)*sin(RadFreq*T));
W = trapz(SK,FK)/Volume;
% i = 1 indicates the code just calculate the loss energy of the.
% solid content = 1.04%, updating parameter i from 1 to 9.
% respectively, rerunning the last three line codes, the loss.
% energy at various solid contents can be obtained.
```

References

[1] D.D.L. Chung, Materials for vibration damping, J. Mater. Sci. 36 (2001) 5733–5738.
[2] W. Fu, D.D.L. Chung, Vibration reduction ability of polymers, particularly polymethylmethacrylate and polytetrafluoroethylene, Polym. Polym. Compos. 9 (2001) 423–426.
[3] R.M. Lin, C. Lu, Modeling of interfacial friction damping of carbon nanotube-based nanocomposites, Mech. Syst. Signal Process. 24 (2010) 2996–3012.
[4] M. Chua, C. Chui, New attenuation predictive model for carbon-based nanocomposites, IEEE Trans. Nanotechnol. 14 (2) (2015) 363–371.
[5] Y. Chen, W. Dong, Parametric studies of nonlinear damping behavior of APS thermal barrier coatings based on cohesive interface model, in: Proc. ASME Turbo Expo, Vol. 7, 2012, pp. 1307–1314, http://dx.doi.org/10.1115/GT2012-69343. Structures and Dynamics, Parts A and B Paper No. GT2012-69343.
[6] Q. Zhu, S. Lu, Modeling of interfacial debonding analysis for reinforced concrete based on ADINA, in: Second International Conference on Information and Computing Science, 2009, pp. 292–295.
[7] D.D.L. Chung, A review of exfoliated graphite, J. Mater. Sci. 51 (2016) 554–568.
[8] D.D.L. Chung, Graphite, J. Mater. Sci. 37 (8) (2002) 1475–1489.
[9] P. Chen, D.D.L. Chung, Viscoelastic behavior of the cell wall of exfoliated graphite, Carbon 61 (2013) 305–312.
[10] D.D.L. Chung, Interface-derived extraordinary viscous behavior of exfoliated graphite, Carbon 68 (2014) 646–652.

[11] P. Chen, D.D.L. Chung, Elastomeric behavior of exfoliated graphite, as shown by instrumented indentation testing, Carbon 81 (2015) 505–513.
[12] Y. Takizawa, D. Wang, D.D.L. Chung, Carbon black and fumed alumina exhibiting high interface-derived mechanical energy dissipation, Carbon 103 (2016) 436–448.
[13] X. Luo, D.D.L. Chung, Flexible graphite under repeated compression studied by electrical resistance measurements, Carbon 39 (7) (2001) 985–990.
[14] X. Luo, D.D.L. Chung, Vibration damping using flexible graphite, Carbon 38 (10) (2000) 1510–1512.
[15] M.S. Dresselhaus, G. Dresselhaus, Intercalation compounds of graphite, Adv. Phys. 51 (1) (2002) 1–186.
[16] D. Guerard, H. Fuzellier, The graphite intercalation compounds and their applications. NATO ASI Series, Series B: Physics, Condens. Syst. Low. Dimens. 253 (1991) 695–707.
[17] S.H. Anderson, D.D.L. Chung, Exfoliation of intercalated graphite, Carbon 22 (3) (1984) 253–263.
[18] A. Celzard, J.F. Mareche, G. Furdin, Modelling of exfoliated graphite, Prog. Mater. Sci. 50 (1) (2005) 93–179.
[19] M.I. Saidaminov, N.V. Maksimova, N.E. Sorokina, V.V. Avdeev, Effect of graphite nitrate exfoliation conditions on the released gas composition and properties of exfoliated graphite, Inorg. Mater. 49 (9) (2013) 883–888.
[20] A. Herold, D. Petitjean, G. Furdin, M. Klatt, Exfoliation of graphite intercalation compounds: classification and discussion of the processes from new experimental data relative to graphite-acid compounds, Mater. Sci. Forum 152–153 (1994) 281–287 (Soft Chemistry Routes to New Materials).
[21] N. Daumas, A. Herold, Relations between phase concept and reaction mechanics in graphite insertion compounds, Comptes Rendus Hebdomadaires des Seances de L'Academie des Sciences, Serie C 268 (1969) 373–382.
[22] M. Heerschap, P. Delavignette, S. Amelinckx, Electron microscope study of interlamellar compounds of graphite with bromine, iodine monochloride and ferric chloride, Carbon 1 (1964) 235–238.
[23] M. Heerschap, P. Delavignette, Electron-microscopy study of the ferric chloride/graphite compound, Carbon 5 (1967) 383–384.
[24] S.H. Anderson, D.D.L. Chung, Exfoliation of single crystal graphite and graphite fibers intercalated with halogens, Synth. Met. 8 (1983) 343–349.
[25] D.D.L. Chung, Intercalate vaporization during the exfoliation of graphite intercalated with bromine, Carbon 25 (3) (1987) 361–365.
[26] A.Y. Malkin, A.I. Isayev, Rheology – Concepts, Methods, & Applications, ChemTec Publishing, Toronto, 2006.
[27] D.L. Johnson, J. Koplik, L.M. Schwartz, New pore size parameter characterizing transport in porous media, Phys. Rev. Lett. 57 (1986) 2564.
[28] X. Hong, D. Wang, D.D.L. Chung, Strong viscous behavior discovered in nanotube mats, as observed in boron nitride nanotube mats, Compos. Part B B91 (2016) 56–64.